



# HHS Public Access

Author manuscript

*IEEE Trans Med Imaging*. Author manuscript; available in PMC 2018 December 01.

Published in final edited form as:

*IEEE Trans Med Imaging*. 2017 December ; 36(12): 2479–2486. doi:10.1109/TMI.2017.2753138.

## Iterative Low-dose CT Reconstruction with Priors Trained by Artificial Neural Network

**Dufan Wu,**

Gordon Center for Medical Imaging, Massachusetts General Hospital and Harvard Medical School, Boston, MA 20114 USA

**Kyungsang Kim,**

Gordon Center for Medical Imaging, Massachusetts General Hospital and Harvard Medical School, Boston, MA 20114 USA

**Georges El Fakhri, and**

Gordon Center for Medical Imaging, Massachusetts General Hospital and Harvard Medical School, Boston, MA 20114 USA

**Quanzheng Li**

Gordon Center for Medical Imaging, Massachusetts General Hospital and Harvard Medical School, Boston, MA 20114 USA

### Abstract

Dose reduction in computed tomography (CT) is essential for decreasing radiation risk in clinical applications. Iterative reconstruction algorithms are one of the most promising way to compensate for the increased noise due to reduction of photon flux. Most iterative reconstruction algorithms incorporate manually designed prior functions of the reconstructed image to suppress noises while maintaining structures of the image. These priors basically rely on smoothness constraints and cannot exploit more complex features of the image. The recent development of artificial neural networks and machine learning enabled learning of more complex features of image, which has the potential to improve reconstruction quality. In this work, K-sparse autoencoder (KSAE) was used for unsupervised feature learning. A manifold was learned from normal-dose images and the distance between the reconstructed image and the manifold was minimized along with data fidelity during reconstruction. Experiments on 2016 Low-dose CT Grand Challenge were used for the method verification, and results demonstrated the noise reduction and detail preservation abilities of the proposed method.

### Index Terms

artificial neural networks; computed tomography; iterative algorithms; k-sparse autoencoder; reconstruction algorithms

---

Personal use of this material is permitted. However, permission to use this material for any other purposes must be obtained from the IEEE by sending a request to [pubs-permissions@ieee.org](mailto:pubs-permissions@ieee.org).

Digital Object Identifier: 10.1109/TMI.2017.2753138

## I. Introduction

X-RAY computed tomography (CT) is one of the most important tools for non-invasive diagnoses in modern medicine. The radiation dose is still relatively high in regular CT scans, which leads to increased risk of radiation-related diseases such as cancer. Thus, low-dose CT has been of great research interests in recent years. The most practical way is to reduce the X-ray tube current, but the reduction of photon flux causes increased noises and artifacts in the reconstructed images, which jeopardize the accuracy of diagnoses [1]. Compared to conventional filtered backprojection (FBP) algorithms, iterative image reconstruction methods have great potential in noise reduction and information preservation, by incorporating photon statistics and prior information of the image to be reconstructed [2–4].

Prior information design has attracted a lot of research interests in last decades. Most of the priors are manually designed to enhance image smoothness and maintain edges. A potential function was designed for the difference between neighboring pixels and minimized under data fidelity. Priors such as total variation (TV) or non-local patch-based priors have shown promising results in CT reconstruction with insufficient data, and some if it has already been deployed in commercial software [5][6].

Other than the manually designed priors, some machine learned priors such as dictionary learning and principal component analysis has also been applied in CT reconstruction [7][8]. The reconstructed images were assumed to lie within a linear manifold trained from normal-dose images. However, medical images usually lie in a highly nonlinear manifold rather than a linear space, and the manifold modeling error may lead to artifacts in reconstructed image [9]. On the other hand, with deep artificial neural networks, it is possible to model the nonlinear manifold more precisely and potentially it could improve the image reconstruction quality because of a more precise knowledge of the normal-dose images.

Autoencoders are widely in data manifold modeling [10–14]. It first uses a neural network to map the data to a latent space which has some designed properties, such as sparsity or following certain distribution. Then another network (usually with symmetry structures) is used to reconstruct the data from the latent space. Because of the high nonlinearity and capacity of neural networks, autoencoders have become one of the most important methods in unsupervised learning.

In this work, we proposed a novel iterative CT reconstruction method based on priors learned by a k-sparse autoencoder [13], which will be further explain in section II-B. The k-sparse autoencoder (KSAE) learned a nonlinear sparse prior from normal-dose CT images reconstructed by FBP. During iterative reconstruction of low-dose data, the distance between the reconstructed images and the learned manifold was minimized along with the data fidelity with separable quadratic surrogate (SQS) algorithm [2]. Since the proposed method was trained in a fully unsupervised way, it has more flexibility and less requirement on training data than image denoising algorithms based on deep neural networks [15–23].

The rest of the paper is organized as follows: section II is the methodology, where the k-sparse autoencoder and reconstruction algorithms will be explained in detail. Section III and

IV are the experimental setup and results using the 2016 Low-dose CT Grand Challenge datasets [24]. Section V is the discussion and conclusion.

## II. Methodology

### A. K-Sparse Autoencoders (KSAE)

Autoencoders can be trained as [25]:

$$E, D = \arg \min \sum_k \|\mathbf{x}_k - D(E(\mathbf{x}_k))\| + \lambda R_f(E(\mathbf{x}_k)) \quad (1)$$

where  $E(\cdot)$  and  $D(\cdot)$  are encoder and decoder respectively,  $\mathbf{x}_k$  are the training samples,  $R_f(\cdot)$  is some designed constrains on the encoded data, and  $\lambda$  is a hyperparameter to balance between the reconstruction precision and prior constrains.

In (1), the encoder  $E(\cdot)$  tries to map the highly intractable probability distribution of  $\mathbf{x}_k$  to some well-defined prior distributions  $R_f(\cdot)$ . The power of the mapping increases with the complexity and capacity of the neural network  $E(\cdot)$ . The decoder  $D(\cdot)$  usually has symmetry structures with  $E(\cdot)$ , which tries to reconstruct  $\mathbf{x}_k$  from the latent space defined by  $R_f(E(\mathbf{x}))$ .

When applying autoencoders to CT image reconstruction, the autoencoders' detail preservation capabilities are more important than its general structure modeling ability. Depends on the success of sparse coding in image restoration and several experimental trials, k-sparse autoencoder was used for the data manifold modeling for low-dose CT reconstruction.

A KSAE was trained as [13]:

$$E, D = \operatorname{argmin} \sum_k \|\mathbf{x}_k - D(E(\mathbf{x}_k))\|_2 \quad (2)$$

$$s. t. \|E(\mathbf{x}_k)\|_0 \leq K$$

where  $K$  is the hyperparameter to control the sparsity of the latent space.

Patch-based fully connected neural networks with ReLU activations were used for both encoder and decoder. ReLU was used for its advantage in edge preservation compared to other activation functions such as tanh and sigmoid [26]. To ensure the sparsity constrain in (2), an extra mask layer was added after  $E(\mathbf{x}_k)$ . It would select the  $K$  largest elements in  $E(\mathbf{x}_k)$  and set all the others to zeros. During the training, the mask was first calculated in each iteration. Then it was considered as a constant during the backpropagation, i.e. gradient calculation. The algorithm was greedy and could converge to local minimum empirically [13]. The structure of the neural network is shown in figure 1.

## B. Problem Modeling

The reconstruction problem was modeled as unconstrained optimization to minimize the distance of the image to the trained manifold along with the data fidelity term [7]:

$$\begin{aligned} \mathbf{x}, \mathbf{y} = \operatorname{argmin} & \left\| \mathbf{A}\mathbf{x} - \mathbf{b} \right\|_{\mathbf{w}}^2 + \beta \sum_m^M \left\| \mathbf{P}_m \mathbf{x} - D(E(\mathbf{y}_m)) \right\|_2^2 \quad (3) \\ \text{s.t.} & \left\| E(\mathbf{y}_m) \right\|_0 \leq K, \quad m = 1, 2, 3, \dots, M \end{aligned}$$

where  $\mathbf{x}$  is the image to be reconstructed,  $\mathbf{y} = (\mathbf{y}_1, \dots, \mathbf{y}_M)$  is the projections of the patches on the manifold trained by the autoencoder.  $\mathbf{P}_m$  is the extraction matrix of the  $m$ th patch.  $\beta$  is the hyperparameter to balance between priors and data fidelity.  $\mathbf{A}$  is the system matrix and  $\mathbf{b}$  is the logarithm sinogram.  $\mathbf{w}$  is a diagonal noise weighting matrix where  $w_{ii} = \exp(-b_i)$ , which assumed a zero electronic noise because there was no information about it.

In (3),  $E(\mathbf{y}_m)$  defined the latent coordinates of the L2 projection of  $\mathbf{P}_m \mathbf{x}$  on the trained manifold. A simplified geometric interpretation of the problem is shown in figure 2. Due to the difficulty of tackling the zero-norm constrain, an indirect latent representation  $E(\mathbf{y}_m)$  was used rather than a direct latent variable.

## C. Optimization Algorithm

It should be noted that (3) is highly non-convex because of the constrains and the structure of  $E(\cdot)$  and  $D(\cdot)$ , thus the solution would be sensitive to the initial point  $\mathbf{x}_0$  and the algorithm. A monotonically non-increasing alternating optimization algorithm was used to solve (3) [7]. Define two sub-problems regarding  $\mathbf{x}$  and  $\mathbf{y}$ :

$$f(\mathbf{x}, \mathbf{y}^n) = \left\| \mathbf{A}\mathbf{x} - \mathbf{b} \right\|_{\mathbf{w}}^2 + \beta \sum_m \left\| \mathbf{P}_m \mathbf{x} - D(E(\mathbf{y}_m^n)) \right\|_2^2 \quad (4)$$

$$\begin{aligned} f(\mathbf{x}^n, \mathbf{y}) &= \left\| \mathbf{A}\mathbf{x}^n - \mathbf{b} \right\|_{\mathbf{w}}^2 + \beta \sum_m \left\| \mathbf{P}_m \mathbf{x}^n - D(E(\mathbf{y}_m)) \right\|_2^2 \quad (5) \\ \text{s.t.} & \left\| E(\mathbf{y}_m) \right\|_0 \leq K \end{aligned}$$

where  $\mathbf{x}^n$  and  $\mathbf{y}^n$  are the  $\mathbf{x}$  and  $\mathbf{y}$  in the  $n$ th iteration respectively.

Separable quadratic surrogate (SQS) algorithm was applied on the convex problem (4):

$$\mathbf{x}^{n+1} = \mathbf{x}^n - \frac{\mathbf{A}^T \mathbf{w} (\mathbf{A}\mathbf{x}^n - \mathbf{b}) + \beta \sum_m \mathbf{P}_m^T (\mathbf{P}_m \mathbf{x}^n - D(E(\mathbf{y}_m^n)))}{\mathbf{A}^T \mathbf{w} \mathbf{A} \mathbf{1} + \beta \sum_m \mathbf{P}_m^T \mathbf{P}_m \mathbf{1}} \quad (6)$$

where  $\mathbf{A}^T$  is the transpose of  $\mathbf{A}$  and refers to backprojection,  $\mathbf{P}_m^T$  is the operation to put the  $m$ th patch back to where it is extracted,  $\mathbf{1}$  is an all-ones vector.

Steepest descend was applied on (5):

$$\mathbf{y}_m^{n+1} = \mathbf{y}_m^n - \alpha \cdot \frac{\nabla \left\| \mathbf{P}_m \mathbf{x}^n - D(E(\mathbf{y}_m)) \right\|_2^2}{\left\| \nabla \left\| \mathbf{P}_m \mathbf{x}^n - D(E(\mathbf{y}_m)) \right\|_2^2 \right\|_2} \Bigg|_{\mathbf{y}_m = \mathbf{y}_m^n} \quad (7)$$

$$s.t. \left\| E(\mathbf{y}_m) \right\|_0 \leq K$$

where  $\alpha$  is the step size. Equation (7) could be repeated for several times with small  $\alpha$  for better convergence. Experimental results showed that proper choice of a fixed  $\alpha$  was enough to decrease  $f(\mathbf{x}^n, \mathbf{y})$  for most of the iterations.

The SQS step (6) guaranteed  $f(\mathbf{x}^{n+1}, \mathbf{y}^n) < f(\mathbf{x}^n, \mathbf{y}^n)$ , and with proper choice of step size  $\alpha$ , (7) would lead to  $f(\mathbf{x}^{n+1}, \mathbf{y}^{n+1}) < f(\mathbf{x}^{n+1}, \mathbf{y}^n)$ . Therefore, alternation between the two steps gave:

$$f(\mathbf{x}^{n+1}, \mathbf{y}^{n+1}) \leq f(\mathbf{x}^{n+1}, \mathbf{y}^n) \leq f(\mathbf{x}^n, \mathbf{y}^n) \quad (8)$$

which indicated that the cost function was monotonically nonincreasing.

To deal with the non-convexity of the problem, several additional techniques were used to avoid bad local minimum and saddle points:

1.  $\mathbf{x}_0$  was selected as the mean of the adjacent 3 layers of the original FBP results, which was one of the simplest way for a better starting point. More recent denoising algorithms could be used but they are currently out of scope of this study.
2. Instead of using fixed patch extraction matrices  $\mathbf{P}_m$ , overlapped patches were extracted from random locations at each iteration. This was similar to the stochastic gradient descend algorithm, where part of the data was used to calculate the gradient each time, which could converge to local minimum and escape saddle points [27][28].
3. Due to the random patch extraction strategy, the cost to keep track of  $\mathbf{y}_m$  was too high. Instead, the initial value of  $\mathbf{y}_m$  was first estimated with:

$$\mathbf{y}_m^{n,0} = D(E(\mathbf{P}_m \mathbf{x}^n)) \quad (9)$$

then several steps of the gradient descend (7) was carried out. 5 steps of (7) with a step size of 0.05 was used in our experiments.

The reconstruction algorithm is summarized in table 1. Nesterov's momentum method [29] was used to accelerate the algorithm.

In table I,  $N_{SD}$  is the step of steepest descend (7) and  $\gamma$  is the parameter for Nesterov's momentum method. Step 4 to 6 were to calculate the projection of the current image  $\mathbf{x}^n$  on the trained manifold, where the gradient was calculated according to (7). Step 7 and 8 were the SQS and momentum acceleration step, where  $SQS(\mathbf{x}^n, \mathbf{y}^n)$  was the second term on the right-hand side of (6). Fixed number of iterations based on experience were used for the stopping criteria.

#### D. Three-Dimensional Reconstruction

Due to the large number of variables in the fully connected neural network, it was impractical to train the autoencoders on 3D patches. Instead, three independent autoencoders were trained from axial, sagittal and coronal slices, and the reconstruction problem was reformed as:

$$\begin{aligned} \mathbf{x}, \mathbf{y} = \operatorname{argmin} & \|\mathbf{A}\mathbf{x} - \mathbf{b}\| \\ & \times \left\| \frac{2}{\mathbf{w}} + \frac{\beta}{3} \sum_{s=1}^3 \sum_{M_s}^m \|\mathbf{P}_{sm} \mathbf{x} - D_s(E_s(\mathbf{Y}_{sm}))\|_2^2 \right. \\ & \left. s.t. \|E_s(\mathbf{Y}_{sm})\|_0 \leq K, \quad s = 1, 2, 3; \quad m = 1, 2, \dots, M_s \right. \end{aligned} \quad (10)$$

where  $s$  stands for one of the three directions.  $\mathbf{P}_{sm}$  is the patch extraction matrix along the  $s$ th direction.  $D_s(\cdot)$  and  $E_s(\cdot)$  are the decoder and encoder trained for the  $s$ th direction respectively.  $M_s$  is the number of patches along the  $s$ th direction.  $\mathbf{y}$  is the collection of all the  $\mathbf{y}_{sm}$ . Equation (10) could also be solved by algorithm 1.

### III. Experimental Setup

#### A. Datasets

The experiments were carried on 2016 Low-dose CT Grand Challenge datasets, which contained projection and image data of the chest and abdomen from 10 different patients. The data were acquired with Siemens Somatom Definition CT scanners, under 120kVp and 200 effective mAs. Quarter-dose data were provided by the challenge committee, which were simulated from the normal-dose data by noise injection. The challenge committee also

provided the FBP results for both normal- and low-doses, where the spatial resolution varied from  $0.66\text{mm} \times 0.66\text{mm}$  to  $0.8\text{mm} \times 0.8\text{mm}$ , with a slice thickness of  $0.8\text{mm}$ .

## B. Training of KSAE

3 independent KSAEs were trained for axial, sagittal and coronal directions, where 1 million  $16 \times 16$  patches were randomly extracted from 5 of the 10 patients' data for each direction. The Hu values of the patches were divided by 500 for better training conditions.

The KSAEs had the structure in figure 1, where 3 fully connect layers with 1024 units was used for both encoder and decoder. 50 epoches of ADAM algorithm with a step size of 0.0001 with other parameters same as in [30]. A minibatch size of 100 was used for the training. A weight decay of 0.1 was also added to stabilize the trained weights [25]. The KSAEs were implemented with tensorflow [31].

## C. Reconstruction Setups

The data from the patients other than the training set were used for reconstruction study. The projections were first rebinned to multi-slice fan beam geometry before reconstruction for computational efficiency [38] as was shown in figure 3. Some key geometry parameters for the original and rebinned data are shown in table 2.

The images were reconstructed with  $0.8 \times 0.8 \times 0.8 \text{ mm}^3$  voxel size, with an axial resolution of  $640 \times 640$  pixels, which was enough to cover the entire field of view (FOV). Ray-driven forward projection and pixel-driven backprojection were used for the iterative reconstruction [32]. The number of iterations was fixed to 50 for reconstruction, which was enough to reach a stable result.

## D. Comparison Study

The widely used TV prior and the dictionary learning based prior were used for comparison studies [5][7]. For the TV prior, the L1-norm of gradients with a regularization factor was used, which lead to differentiable cost functions:

$$\mathbf{x} = \operatorname{argmin} \|\mathbf{Ax} - \mathbf{b}\|_{\mathbf{w}}^2 + \beta \sum_j \sum_{k \in \mathcal{N}_j} \frac{1}{2} \sqrt{(x_j - x_k)^2 + \delta} \quad (11)$$

where  $\mathcal{N}_j$  is the 4- or 6-neighbourhood of pixel  $j$ ,  $\delta = 10^{-6}$ . Problem (11) was solved via the SQS algorithm.

The dictionary learning prior was similar to (3):

$$\mathbf{x}, \mathbf{h} = \operatorname{argmin} \left\| \mathbf{A}\mathbf{x} - \mathbf{b} \right\|_{\mathbf{w}}^2 + \beta \sum_m^M \sum_{M_s}^m \left\| \mathbf{P}_m \mathbf{x} - \mathbf{D}\mathbf{h}_m \right\|_2^2 \quad (12)$$

$$s.t. \left\| \mathbf{h}_m \right\|_0 \leq K, \quad s = 1, 2, 3; \quad m = 1, 2, \dots, M$$

where  $\mathbf{h} = (\mathbf{h}_1, \mathbf{h}_2, \dots, \mathbf{h}_M)$  is the coefficients for the dictionary on each patch.  $\mathbf{D}$  is a global dictionary trained with KSVD [33] on the same training set with the KSAE. The number of elements in the dictionary was set to 1024. A smaller dictionary trained on  $8 \times 8$  patches was also tried, but it was outperformed by the dictionary trained on  $16 \times 16$  patches. Problem (12) was also optimized with algorithm 1, where the gradient descend step 6 and 7 was replaced with orthogonal matching pursuit (OMP) [34]. All the techniques for non-convex optimization proposed to solve (3) was also applied on (12). The 3D realization of dictionary learning prior was in the same format with (10). KSVD and OMP were realized with SPAMS [35].

## IV. Experimental Results

### A. Algorithm Verification

To verify that algorithm 1 could indeed minimize (3), 200 iterations were run to investigate the change of the total cost function and prior term under different hyperparameters. There was a peak on the total loss curve in early iterations which was due to the momentum acceleration, but the algorithm was converging overall. The prior term loss was also decreasing with increased hyperparameter  $\beta$  as expected. For the reconstructions in the following sections, the iterations were truncated at 50.

### B. Determination of Hyperparameters

A single slice as shown in figure 5 was used to determine the hyperparameters  $\beta$  and  $K$ . The FBP results from normaldose image was used as the reference image to calculate the structural similarity index (SSIM) [36] of a region near liver. The SSIM was used as the primary indicator of reconstruction quality to determine the optimal hyperparameter. The value of the images was cropped to  $40 \text{ HU} \pm 200 \text{ HU}$  when calculating the SSIM so that the high-density bones would not cause significant impact on the SSIM.

To investigate the algorithms' ability of recovering lesions in the liver, the contrast to noise ratio (CNR) was also calculated from the lesion highlighted with the white box in figure 5. The mask for the lesion and background areas were the shared across low-dose reconstruction results. A separate segmentation was used for the normal-dose FBP, because of some noticeable structural difference between low-dose and normal-dose results.

The SSIM- $\beta$  and SSIM-CNR curves of the reconstructed results are shown in figure 6. For KSAE and dictionary learning, the sparsity level  $K$  was basically determined by the peak SSIM. However,  $K = 90$  for KSAE and  $K = 30$  for dictionary learning were unstable with regard to  $\beta$  and they were not used for the reconstruction of other cases.  $K$  was selected as



100 and 40 for KSAE and dictionary learning respectively.  $\beta$  was selected as 5, 7, and 0.00125 for KSAE, dictionary and TV, respectively.

In figure 6 (d), the SSIM-CNR curve demonstrated that TV emphasized on structural preservation, whereas dictionary learning had some advantage of noise suppression. KSAE had the best overall peak performance among the 3 algorithms for the selected slice.

### C. Quarter-dose Reconstruction Results

The algorithms were applied on the quarter-dose data provided by the Low-dose Challenge committee and the reconstruction results are shown in figure 7 to 9. SSIMs were calculated for regions that contained liver, and CNRs were calculated for the lesions. Furthermore, to evaluate the texture preservation ability, the 13 Haralick texture features [39][40][41] were calculated for each result inside the ROI, and the normalized distance to the full-dose FBP's features:

$$L(\mathbf{x}, \mathbf{x}_{FBP}) = \sqrt{\sum_i \left( \frac{h_i(\mathbf{x}) - h_i(\mathbf{x}_{FBP})}{h_i(\mathbf{x}_{FBP})} \right)^2} \quad (13)$$

where  $h_i(\mathbf{x})$  stands for the  $i$ th components of the Haralick texture features of  $\mathbf{x}$ .

The corresponding results are listed in table 3. The proposed KSAE algorithm could achieve the best quantitative indicators for most of the cases, except for case 3 (figure 9), where TV achieved better SSIM mainly because of its better smoothness in the flat region.

Figure 7 gave the 3D reconstruction results, where the 3-layer mean of quarter-dose FBP images were used as  $\mathbf{x}_0$  for the reconstruction algorithms, which provided a relatively good start point for the non-convex dictionary learning and KSAE algorithms. There was no obvious blurring and artifacts induced by the reconstruction algorithms in the sagittal and coronal views.

In figure 9, there was a lesion-like artifact in the quarter-dose images (yellow arrow 3) near the benign cyst (white arrow 2), which was not presented in the normal-dose FBP result. The CNR for this artifact was also calculated and KSAE achieved the lowest score. The artifact was very similar to the benign cyst in the results of TV and dictionary learning, but its visibility was much lower in the KSAE result.

### D. Lower-dose Reconstruction Results

To study the stability of the proposed algorithm and investigate its dose reduction limit, lower-dose data was generated by angular subsampling from the quarter-dose data. A portion of projections uniformly distributed across  $360^\circ$  was removed for further dose reduction. Although this approach would lead to non-uniform angular sampling such as missing 1 projection every 4 projections, no obvious artifacts were observed in the FBP results because of the original dense angular sampling rate (2304 samples per rotation) and strong noises in the images.

1/6, 1/4, 1/3, and 1/2 samples were reduced from the quarter-dose data of the slice in figure 5, the SSIMs and CNRs of the reconstructed results are shown in figure 10. The same hyperparameters used for the quarter-dose reconstruction were used. It could be observed that KSAE kept the best performance until 1/3 sample reduction, which was equivalent to 1/6 of the normal-dose. The reconstruction results of KSAE are shown in figure 12. It could be observed from both the CNR curve and the reconstructed results that when the half of the samples were reduced, the lesion became barely visible.

Figure 11 demonstrated the SSIMs of the reconstructed results with different hyperparameters under various dose. With lower dose, the different between large  $\beta$  and the peak performance  $\beta$  vanished, because of the increased demand in noise control during reconstruction. The performance of larger  $K$  also deteriorated due to the fact that larger  $K$  had less constraints on the trained manifold and noises would be included in the reconstructed images. There was no dramatical changes on the curves, which indicated the stability of both  $K$  and  $\beta$  for different dose level.

## V. Conclusion and Discussion

In this paper, an unsupervised learning method was proposed to train a prior function for iterative low-dose CT reconstruction with  $K$ -sparse autoencoders. Alternating optimization and SQS was used to solve the problem with several techniques applied to deal with the non-convexity. Experimental results on 2016 Low-dose CT Challenge data demonstrated that KSAE prior could achieve better performance than dictionary learning and total variation for quarter-dose data, with better noise suppression and structural preservation. The proposed algorithm could still achieve acceptable performance until 1/6 dose.

The machine learning methods demonstrated a more uniform noise patterns in the reconstruction results compared to TV. But the manifold modeling bias may lead to a deteriorated performance on SSIMs, especially for low contrast structures in livers. Both KSAE and dictionary learning used sparse assumptions on the latent space, but with deep structures and nonlinear mapping functions, KSAE could achieve more precise manifold description and lead to better performance on noise reduction and structural preservation. In figure 13 we demonstrated the SSIMs of the reconstruction results with different number of layers for both encoders and decoders, which indicated that deeper structures increased the performance of the prior.

In the study, it was noticed that the optimal sparsity level  $K$  for KSAE was much larger than that in the dictionary learning. one of the possible reason was for a more complicated manifold modeled by the neural network, more variables were needed to describe it.

In this study, the dataset from the low-dose challenge was simulated with noise injection, which could be different from real situations. But since the KSAE was trained in an unsupervised way and no knowledge on the noise property was assumed during the training, the method should be still applicable to real data. The application of the method on real data and more rigorous evaluation of the results other than SSIMs and CNRs would be one of our future works.

One big issue raised with the neural network was the dramatically increased parameters of the algorithm. Besides obvious parameters such as  $\beta$ ,  $K$ , depth of autoencoders and patch size, optimal network structure is also an open question. We demonstrated the feasibility of manifold modeling with  $K$ -sparse autoencoders constructed by fully connected neural networks, but the feasibility of other neural network structures and assumptions on the latent space are yet to be explored. Theoretically, given enough data, deeper neural network with higher capacity could always yield better results. However, as an unsupervised learning method, the design of the constraints on the latent space is an even more crucial issue, which needs further studies and explorations.

## Acknowledgments

Thanks the 2016 Low-dose CT Grand Challenge provided valuable datasets for this study.

This work was supported in part by the National Institutes of Health under Grant R01EB013293 and R01AG052653.

## References

1. Kalra MK, Maher MM, Toth TL, et al. Strategies for CT radiation dose optimization 1. *Radiology*. 2004; 230(3):619–628. [PubMed: 14739312]
2. Erdogan H, Fessler JA. Monotonic algorithms for transmission tomography. *IEEE Transactions on Medical Imaging*. 1999; 18(9):801–814. [PubMed: 10571385]
3. Prakash P, Kalra MK, Kambadakone AK, et al. Reducing abdominal CT radiation dose with adaptive statistical iterative reconstruction technique. *Investigative Radiology*. 2010; 45(4):202–210. [PubMed: 20177389]
4. Pickhardt PJ, Lubner MG, Kim DH, et al. Abdominal CT with model-based iterative reconstruction (MBIR): initial results of a prospective trial comparing ultralow-dose with standard-dose imaging. *American Journal of Roentgenology*. 2012; 199(6):1266–1274. [PubMed: 23169718]
5. Sidky EY, Pan X. Image reconstruction in circular cone-beam computed tomography by constrained, total-variation minimization. *Physics in Medicine and Biology*. 2008; 53(17):4777–4807. [PubMed: 18701771]
6. Kim K, Ye JC, Worstell W, et al. Sparse-view spectral CT reconstruction using spectral patch-based low-rank penalty. *IEEE Transactions on Medical Imaging*. 2015; 34(3):748–760. [PubMed: 25532170]
7. Xu Q, Yu H, Mou X, et al. Low-dose X-ray CT reconstruction via dictionary learning. *IEEE Transactions on Medical Imaging*. 2012; 31(9):1682–1697. [PubMed: 22542666]
8. Wu D, Li L, Zhang L. Feature constrained compressed sensing CT image reconstruction from incomplete data via robust principal component analysis of the database. *Physics in Medicine and Biology*. 2013; 58(12):4047–4070. [PubMed: 23685849]
9. Kingma DP, Max W. Auto-encoding variational bayes. arXiv preprint. 2013 arXiv:1312.6114.
10. Vincent P, Larochelle H, Bengio Y, et al. Extracting and composing robust features with denoising autoencoders. *Proceedings of the 25th International Conference on Machine Learning*. 2008:1096–1103.
11. Ng A. Sparse autoencoder. CS294A Lecture notes. 2011:1–19. 72.2011.
12. Masci J, Meier U, Cire an D, Schmidhuber J. Stacked convolutional auto-encoders for hierarchical feature extraction. *Artificial Neural Networks and Machine Learning–ICANN 2011*. 2011:52–59.
13. Makhzani A, Brendan FJ. Winner-take-all autoencoders. *Advances in Neural Information Processing Systems*. 2015
14. Larsen ABL, Søren SK, Larochelle H, Winther O. Autoencoding beyond pixels using a learned similarity metric. arXiv preprint. 2015 arXiv:1512.09300.

15. Burger HC, Schuler CJ, Harmeling S. Image denoising: Can plain neural networks compete with BM3D? 2012 IEEE Conference on Computer Vision and Pattern Recognition (CVPR). 2012:2392–2399.
16. Xie J, Xu L, Chen E. Image denoising and inpainting with deep neural networks. *Advances in Neural Information Processing Systems*. 2012:341–349.
17. Kang E, Min J, Ye JC. A deep convolutional neural network using directional wavelets for low-dose X-ray CT reconstruction. *arXiv preprint*. 2016 arXiv:1610.09736.
18. Ledig C, Theis L, Huszár F, et al. Photo-realistic single image super-resolution using a generative adversarial network. *arXiv preprint*. 2016 arXiv:1609.04802.
19. Jin KH, McCann MT, Froustey E, Unser M. Deep convolutional neural network for inverse problems in imaging. *IEEE Transactions on Image Processing*. 2016; 26(9):4509–4522.
20. Wang S, Su Z, Ying L, et al. Accelerating magnetic resonance imaging via deep learning. 2016 IEEE 13th International Symposium on Biomedical Imaging (ISBI). 2016:514–517.
21. Chen H, Zhang Y, Kalra MK, et al. Low-Dose CT with a Residual Encoder-Decoder Convolutional Neural Network (RED-CNN). *arXiv preprint*. arXiv:1702.00288.
22. Chen H, Zhang Y, Zhang W, et al. Low-dose CT via convolutional neural network. *Biomedical optics express*. 2017; 8(2):679–694. [PubMed: 28270976]
23. Wolterink JM, Leiner T, Viergever MA, Isgum I. Generative Adversarial Networks for Noise Reduction in Low-Dose CT. *IEEE Transactions on Medical Imaging*. 2017 Accepted.
24. AAPM. Low Dose CT Grand Challenge. 2016 Aug. [Online] Available online: <http://www.aapm.org/GrandChallenge/LowDoseCT/>
25. Goodfellow, I., Bengio, Y., Courville, A. *Deep learning*. MIT press; 2016.
26. Krizhevsky A, Sutskever I, Hinton GE. Imagenet classification with deep convolutional neural networks. *Advances in neural information processing systems*. 2012:1097–1105.
27. Bottou L. Large-scale machine learning with stochastic gradient descent. *Proceedings of COMPSTAT'2010*. 2010:177–186.
28. Ge R, Huang F, Jin C, Yuan Y. Escaping from saddle points—online stochastic gradient for tensor decomposition. *Conference on Learning Theory*. 2015:797–842.
29. Devolder O, Glineur F, Nesterov Y. First-order methods of smooth convex optimization with inexact oracle. *Mathematical Programming*. 2014; 146(1–2):37–75.
30. Kingma D, Ba J. Adam: A method for stochastic optimization. *arXiv preprint*. 2014 arXiv:1412.6980.
31. Abadi M, Agarwal A, Barham P, et al. Tensorflow: Large-scale machine learning on heterogeneous distributed systems. *arXiv preprint*. 2016 arXiv:1603.04467.
32. Zeng GL, Gullberg GT. Unmatched projector/backprojector pairs in an iterative reconstruction algorithm. *IEEE Transactions on Medical Imaging*. 2000; 19(5):548–555. [PubMed: 11021698]
33. Aharon M, Elad M, Bruckstein A. K-SVD: An algorithm for designing overcomplete dictionaries for sparse representation. *IEEE Transactions on signal processing*. 2006; 54(11):4311–4322.
34. Tropp JA, Gilbert AC. Signal recovery from random measurements via orthogonal matching pursuit. *IEEE Transactions on information theory*. 2007; 53(12):4655–4666. Online Available: <http://spams-devel.gforge.inria.fr/>.
35. Wang Z, Bovik AC, Sheikh HR, et al. Image quality assessment: from error visibility to structural similarity. *IEEE Transactions on Image Processing*. 2004; 13(4):600–612. [PubMed: 15376593]
36. Ramani S, Fessler JA. A splitting-based iterative algorithm for accelerated statistical X-ray CT reconstruction. *IEEE Transactions on Medical Imaging*. 2012; 31(3):677–688. [PubMed: 22084046]
37. Noo F, Defrise M, Clackdoyle R. Single-slice rebinning method for helical cone-beam CT. *Physics in Medicine and Biology*. 1999; 44(2):561–570. [PubMed: 10070801]
38. Haralick RM, Shanmugam K. Textural features for image classification. *IEEE Transactions on systems, man, and cybernetics*. 1973; SMC-3(6):610–621.
39. Coelho LP. Mahotas: Open source software for scriptable computer vision. *Journal of Open Research Software*. 2013; 1(1)

40. Zhang H, Han H, Liang Z, et al. Extracting information from previous full-dose CT scan for knowledge-based Bayesian reconstruction of current low-dose CT images. *IEEE Transactions on Medical Imaging*. 2016; 35(3):860–870. [PubMed: 26561284]

Author Manuscript

Author Manuscript

Author Manuscript

Author Manuscript

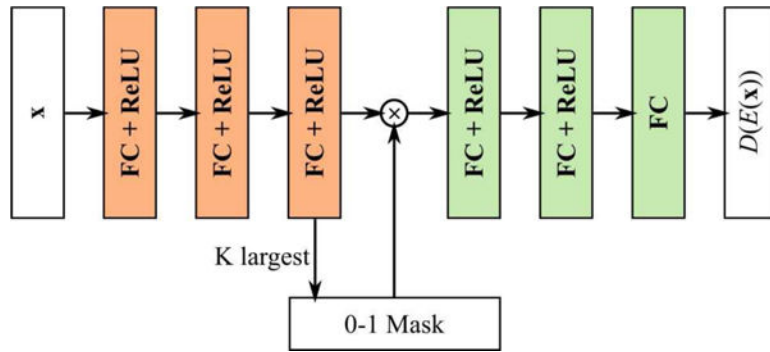


**Fig. 1.**

The structure of the k-sparse neural network. FC stands for fully connected layers. The orange blocks are the encoder  $E(\cdot)$  and the green blocks are the decoder  $D(\cdot)$ . Three layers were demonstrated for both encoder and decoder, but the number of layers may vary. The mask was only updated during forward propagation and considered as constant during backpropagation.

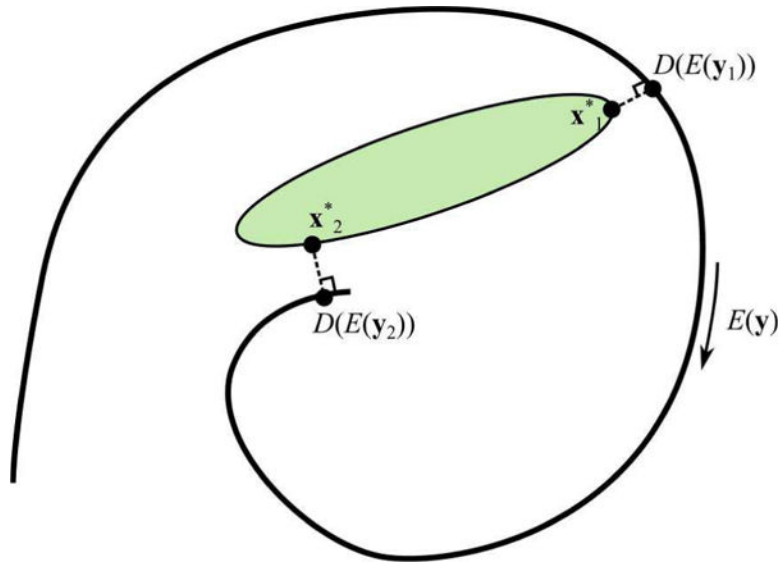


**Fig. 2.** The geometric interpretation of the reconstruction algorithm. The solid spiral represents the trained manifold, which has a coordinate system defined by  $E(\mathbf{y})$ . The green ellipse is the data feasible domain. The optimization would minimize the distance between the feasible domain and the manifold, which could converge to either  $\mathbf{x}_1^*$  or  $\mathbf{x}_2^*$ , depending on the starting point and the algorithm. Constrained optimization concept is used here for better demonstration.

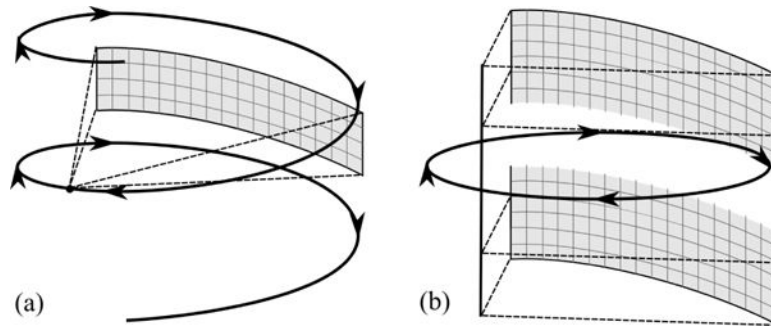


**Fig. 3.** Projection rebinning: (a) the helical geometry before rebinning, there was also a flying focal spot during scanning; (b) the multi-slice fan-beam geometry after rebinning.



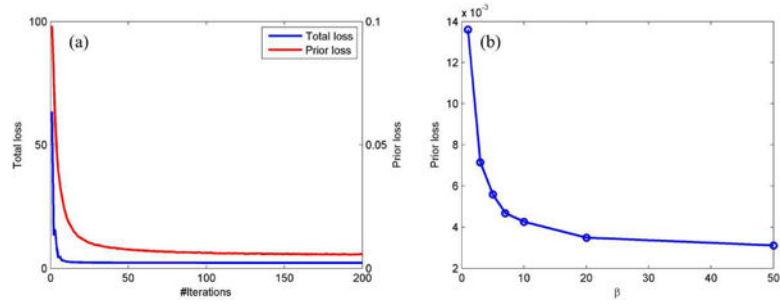


**Fig. 4.** The convergence curve for algorithm 1: (a) The total loss and prior term loss under different iterations with  $\beta = 5$  and  $K = 100$ . (b) The prior loss at 200th iteration for different  $\beta$ s.

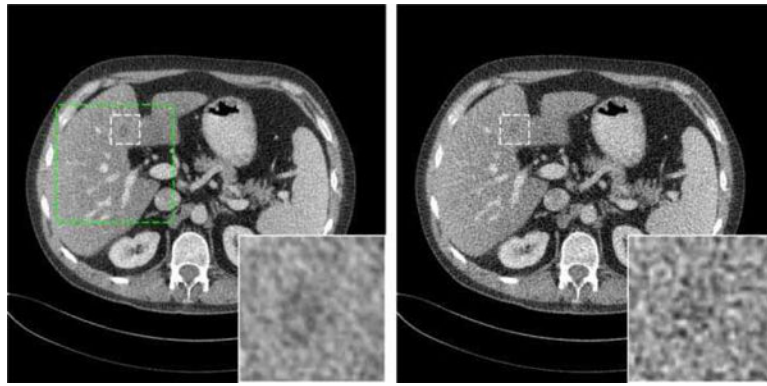


**Fig. 5.** FBP results from normal-dose (left) and quarter-dose (right) data of the selected slice. The quarter-dose result was the mean of 3 adjacent slices. A metastasis was highlighted with the dashed white boxes and zoomed in. The SSIM was calculated using the region inside the big green box. Display window was  $40 \text{ HU} \pm 200 \text{ HU}$ .

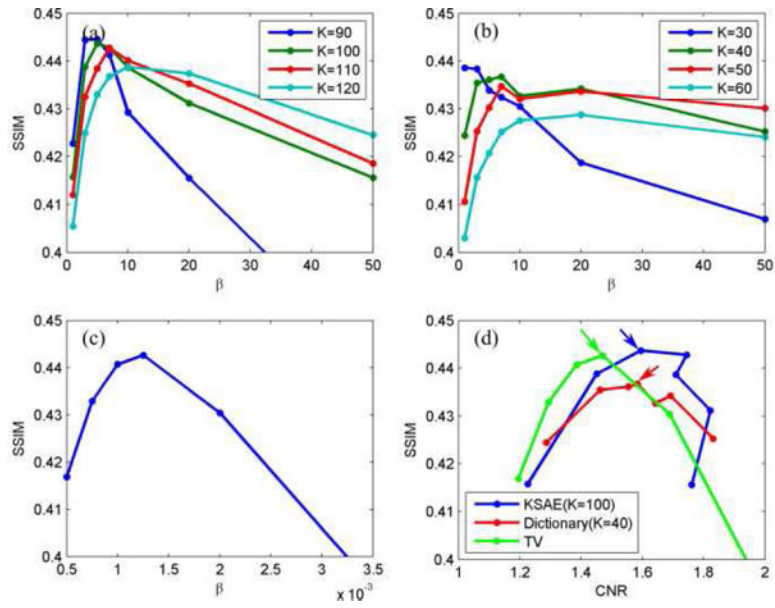


**Fig. 6.** The SSIM- $\beta$  and SSIM-CNR curves for the selected slice: (a) KSAE; (b) Dictionary learning; (c) TV; (d) SSIM-CNR curve for the selected  $K$  of KSAE and dictionary learning. The points used for the other reconstructions were marked with arrows for each algorithm.

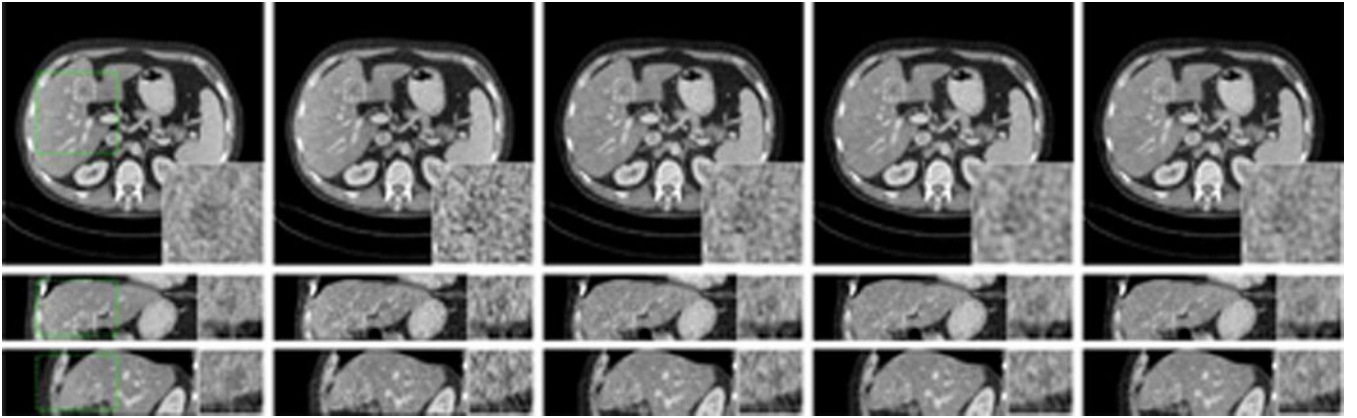


**Fig. 7.**

3D Reconstruction results of case 1 with metastasis. The quarter-dose FBP results were the mean of 3 adjacent layers. The SSIMs were calculated as the mean of the slice-wise SSIMs inside the big green box. The Haralick features were also calculated in the green box. The CNR of the lesion was calculated for the displayed axial layer. The display window is  $40 \text{ HU} \pm 200 \text{ HU}$ .

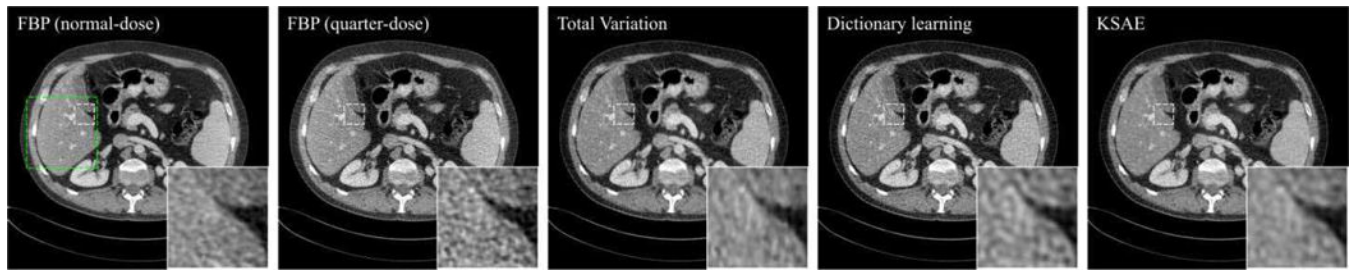


**Fig. 8.**  
2D Reconstruction results of case 2 with focal fat/focal fatty sparing. The display window is  $40 \text{ HU} \pm 200 \text{ HU}$ .

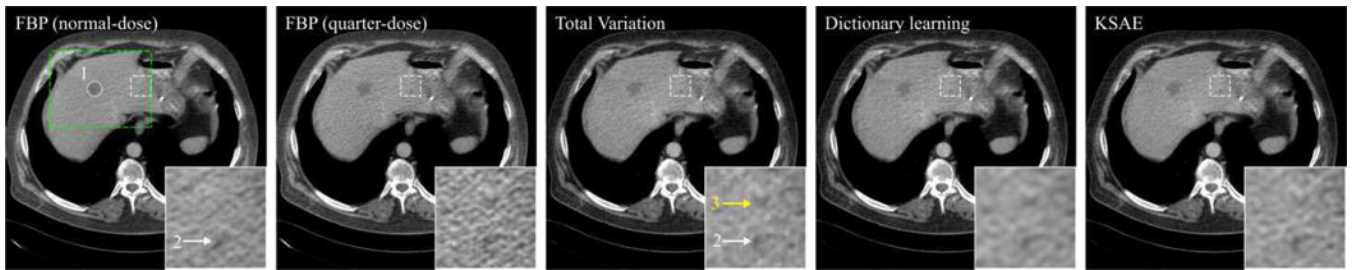


**Fig. 9.** 2D reconstruction results of case 3 with metastasis (white circle) and benign cyst (arrow 2). There is also a false positive lesion on low-dose reconstruction results marked with the yellow arrow 3. The display window is  $40 \text{ HU} \pm 200 \text{ HU}$ .

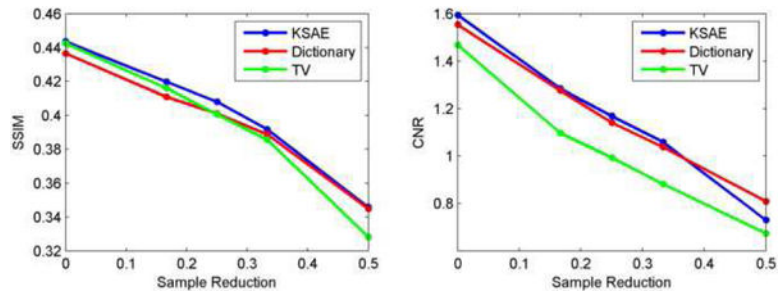


**Fig. 10.** SSIMs and CNRs of the reconstructed test slice given different sample reduction rate from quarter-dose data. The hyperparameters were the same with that in section IV. C.

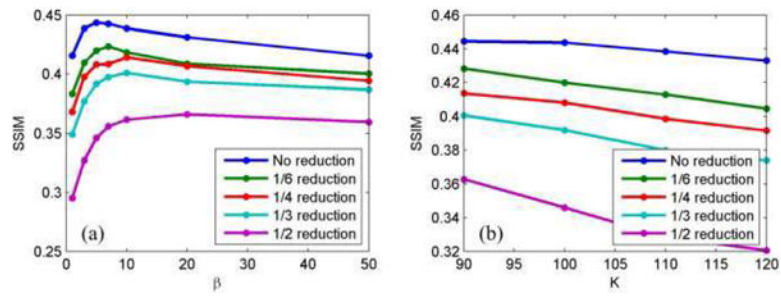


**Fig. 11.** SSIMs of KSAE reconstructed test slice given various hyperparameters under different doses: (a) SSIM- $\beta$  curves for  $K = 100$ ; (b) SSIM- $K$  curves for  $\beta = 5$ .



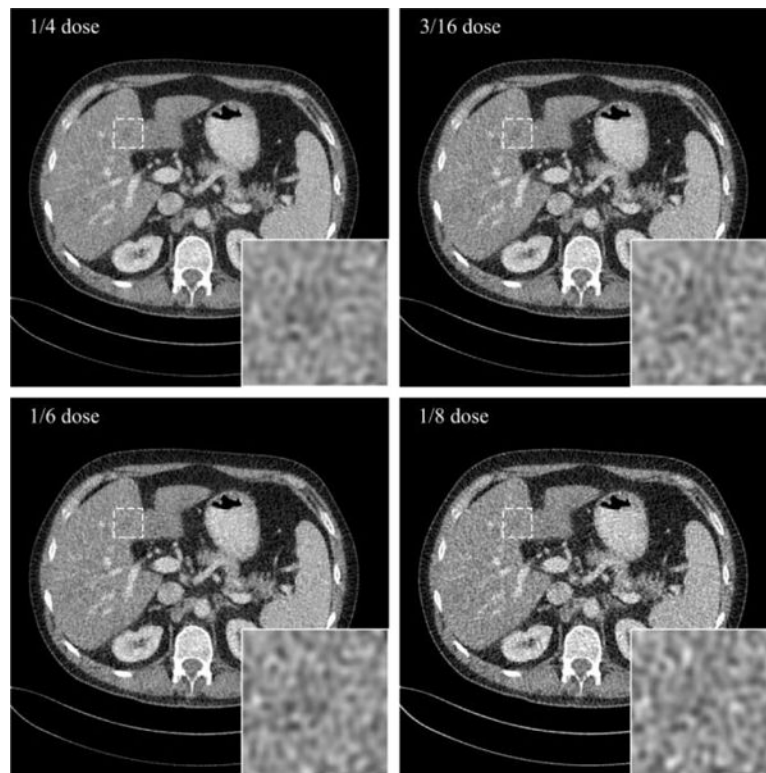


**Fig. 12.** The KSAE reconstruction results under different dose achieved by subsampling from quarter-dose projections. The metastasis was barely visible under half sampling, which was equivalent to 1/8 dose.

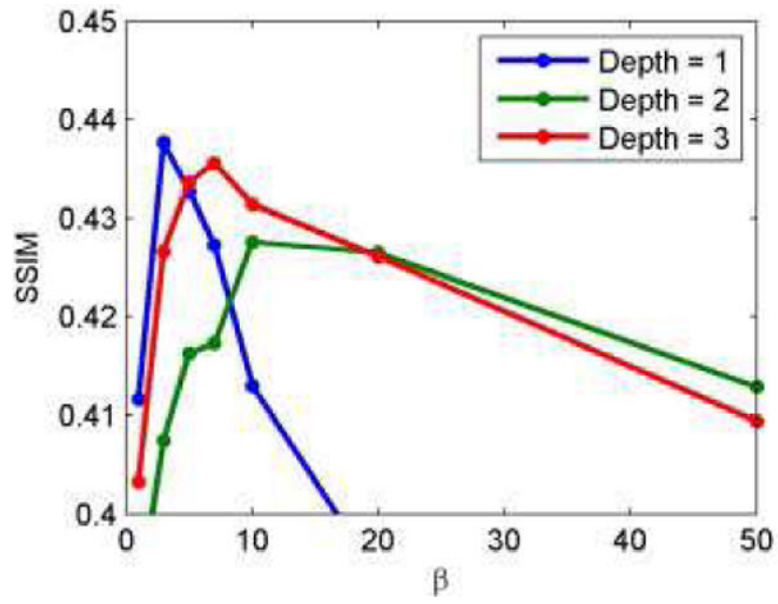


**Fig. 13.** SSIMs of the KSAE reconstructed quarter-dose results with different depth of neural network. The hyperparameters were  $K = 100$  and  $\beta = 5$ .

TABLE I

## Reconstruction Algorithm

---

**Algorithm 1. Optimization algorithm for (3)**

---

- 1 Initialize  $\mathbf{x}^0$  from FBP,  $\alpha = 0.05$ ,  $N_{SD} = 5$ ,  $\gamma = 0.5$ . Select  $\beta$ ;
- 2 Let  $\mathbf{z}^0 = \mathbf{x}^0$ ,  $n = 0$ ;
- 3 Repeat until stop:
- 4     Randomly select  $M$  overlapped  $\mathbf{P}_m$
- 5     For each  $m$ ,  $\mathbf{y}_m^n = D(E(\mathbf{P}_m \mathbf{x}^n))$ ;
- 6     For  $k = 1:N_{SD}$  do:
- 7         For each  $m$ ,  $\mathbf{y}_m^k \leftarrow \mathbf{y}_m^n - \alpha \cdot \text{Grad}(\mathbf{x}^n, \mathbf{y}_m^n)$ , according to (7);
- 8      $\mathbf{x}^{n+1} = \mathbf{z}^n - \text{SQS}(\mathbf{x}^n, \mathbf{y}^n)$ , according to (6)
- 9      $\mathbf{z}^{n+1} = \mathbf{x}^{n+1} + \gamma(\mathbf{x}^{n+1} - \mathbf{x}^n)$
- 10     $n \leftarrow n + 1$

---

TABLE II

## Data geometry

Parameter	Original geometry	Rebinned geometry
Views per rotation	2304	2304
Detector resolution	736 × 64	736 per slice
Pixel size	1.2858 × 1.0947 mm <sup>2</sup>	1.2858 × 1.0 mm <sup>2</sup>
Source-center distance	595 mm	595 mm
Source-detector distance	1085.6 mm	1085.6 mm
Pitch	0.6 - 0.8	N/A
Flying focal spot	Yes	No

Author Manuscript

Author Manuscript

Author Manuscript

Author Manuscript

TABLE III

Quantitative Quality

Algorithm	Case 1 (3D)			Case 2			Case 3				
	SSIM	Haralick	CNR	SSIM	Haralick	CNR	SSIM	Haralick	CNR1	CNR2	CNR3 (Artifacts)
Normal-dose FBP	1.000	0.000	1.759	1.000	0.000	1.651	1.000	0.000	2.482	3.449	N/A
Quarter-dose FBP	0.420	0.433	1.223	0.382	0.541	0.935	0.381	0.531	1.648	1.669	0.942
TV	0.483	0.103	1.379	0.443	0.213	1.672	<b>0.522</b>	0.148	1.951	2.708	1.274
Dictionary Learning	0.485	0.113	1.547	0.441	0.111	1.689	0.502	0.175	2.012	2.552	1.370
KSAE	<b>0.493</b>	<b>0.079</b>	<b>1.589</b>	<b>0.446</b>	<b>0.074</b>	<b>1.706</b>	0.509	<b>0.140</b>	<b>2.123</b>	<b>2.800</b>	<b>0.863</b>